Effect of Oxygen Partial Pressure and B_2O_3 on Crystallization Behavior of Phosphorus- and Iron-Containing Phases in a CaO–SiO$_2$–Fe$_2$O$_3$–P$_2$O$_5$ Melt

JUNCHENG LI, GUOXUAN LI, JINSHAN LIANG, DONG GUAN, JINGWEI LI, YANLING ZHANG, SHAOWEN WU, SEETHARAMAN SRIDHAR, and ZUSHU LI

To help maintain the sustainability of the steel industry by improving slag utilization, we are developing a novel process to recover P and Fe from steelmaking slag by controlling oxygen partial pressure and adding slag modifier B_2O_3, to control the precipitation of targeted phases. In this paper, the precipitated phases of the molten synthetic CaO–SiO$_2$–FeO–P$_2$O$_5$(–B$_2$O$_3$) slags were predicted through thermodynamic calculations using FactSage 8.1. A confocal laser scanning microscope (CLSM) was used to in situ observe the crystallization behavior of the targeted metal oxides in the slags. It was found that iron and phosphorus could be recovered in the form of magnetite (Fe$_3$O$_4$) and calcium phosphate (Ca$_{10}$P$_6$O$_{25}$) phases by controlling oxygen partial pressure and adding slag modifier B_2O_3. By changing oxygen partial pressure from 0.21 to 10^{-6} atm, the iron-containing phase transformed from Ca$_2$Fe$_2$O$_5$ to magnetite (Fe$_3$O$_4$). Through the introduction of B_2O_3 from 2 to 8 pct, the amount of calcium phosphate (Ca$_{10}$P$_6$O$_{25}$) first increased and then decreased, with the maximum of 28 pct (*e.g.* 28/100 g slag studied) at 6 pct B_2O_3.

I. INTRODUCTION

STEELMAKING slag, about 15 pct of the crude steel output, is the primary solid waste in the steel industry.[1,2] During the steelmaking process, the slag is crucial for steel chemistry control and thermal insulation. Amongst the key reactions in the steelmaking process is de-phosphorization, and high dephosphorization ability and reasonable melting point are indispensable properties of steelmaking slag. However, phosphate-enriched phases in steelmaking slags hinder its recovery and utilization since phosphorus may reverse to the hot metal.[3] In order to treat and reuse the accumulated steelmaking slag in an environmentally friendly way, various technologies have been developed, such as flotation,[4] magnetic separation,[5] supergravity separation,[6–8] reduction,[9–11] and a three-stage continuous selective process (selective enrichment-selective growth-selective separation),[12–14] to extract phosphate from steelmaking slag. The above-mentioned technologies provide, to some degree, a better understanding of the phosphorus-containing phase formation and its removal from steelmaking slag, and the three-stage continuous selective process is regarded as the most promising process due to its high efficiency and low waste emission. The three-stage-continuous selective process to extract phosphate from steelmaking slag involves the following steps: (1) optimizing the chemical composition of molten slag to promote the enrichment of the targeted phosphorus-rich phase; (2) controlling temperature to promote the crystallization and growth of the phosphorus-rich particles; (3) separating the phosphorus-rich phases from slag according to the difference in physical and chemical properties between phosphorus-rich particles and slag residuals, such as density and magnetic field strength. Of the three steps, the first step is key since it determines the quality of the phosphorus-rich phases and the complexity of subsequent technical steps. Various additives have

JUNCHENG LI, GUOXUAN LI, JINSHAN LIANG and DONG GUAN are with the School of Material Science and Engineering, Jiangsu University, Zhenjiang, Jiangsu Province, 212013 P.R. China. Contact e-mail: leejc2011@163.com JINGWEI LI is with the School of Materials Science and Engineering, Hefei University of Technology, Anhui, 230009, P.R. China. YANLING ZHANG and SHAOWEN WU are with the State Key Laboratory of Advanced Metallurgy, University of Science and Technology Beijing, Beijing, 100083, P.R. China. SEETHARAMAN SRIDHAR is with the School for Engineering of Matter, Transport and Energy, Arizona State University Tempe, AZ 85287. ZUSHU LI is with the WMG, the University of Warwick, Coventry, CV4 7AL, UK.

been applied for optimizing molten slag chemistry to facilitate the generation of phosphorus-rich phases, as summarized in Table I.[15–22] Although phosphorus-rich phases were obtained by these processes, the P_2O_5 content in the phosphorus-rich phases was less than 20 pct, particularly for the slag with basicity (CaO/SiO_2) above 2.0.[15,23] Furthermore, the above-mentioned processes require a large amount of additives and significant energy consumption. It is therefore necessary to explore a more efficient additive to modify the steelmaking slag to obtain the phosphorus-richer phase, for example, calcium phosphate ($Ca_{10}P_6O_{25}$). It is well known that B_2O_3 addition greatly affects the liquidus temperature,[24,25] surface tension,[26] viscosity,[27–29] structure[30–32] and crystallization behaviors[33,34] of common metallurgical slags, including blast furnace slag, steelmaking slag, mold slag, *etc*. Because of its acidic nature, B_2O_3 can be used to modify steelmaking slag by reacting with CaO to generate $Ca_2B_2O_5$. Therefore, it can be reasonably expected that a small amount of B_2O_3 addition can influence the physicochemical property of steelmaking slag and restrict the precipitation of nC_2S-C_3P solid solution to obtain the phosphorus-rich phase (calcium phosphate) efficiently. Furthermore, it has been verified by many investigations[35–37] that the oxidation state of iron depends on oxygen partial pressure, and it is meaningful to obtain the magnetite (Fe_3O_4) phase for the purpose of recovering iron resource from steelmaking slag by magnetic separation.

In this study, a method is explored to simultaneously recover iron and phosphorus from CaO–SiO_2–FeO–P_2O_5 slag by oxygen partial pressure control and B_2O_3 addition. FactSage 8.1 calculations and confocal laser scanning microscope (CLSM) are employed to predict the precipitated phases and to in situ observe the crystallization behavior of slags, respectively. The effect of oxygen partial pressure and B_2O_3 on crystallization behavior of molten slag is discussed.

II. MATERIAL AND METHODS

A. Materials and Sample Preparation

The chemical composition of synthetic slags is presented in Table II and the P_2O_5 content in all slags is 10 pct. The chemical reagents of CaO and SiO_2 were dried at 1000 °C for 4 hours under Ar atmosphere to remove the small amount of volatiles and hydrones. The synthetic slags were made in a platinum crucible by heating the mixtures of chemical reagents of CaO, SiO_2, FeO, P_2O_5 and B_2O_3 at 1600 °C in a vertical tube furnace for 2 hours under high purity Ar atmosphere (with flow rate 0.5 L/min, 99.999 pct), and then the slag samples were rapidly quenched into water. Finally, the quenched slag sample was ground for the experiment.

B. Experimental Apparatus and Procedure

In this study, the crystallization event was observed in situ under the CLSM (SVF-SP; Yonekura MFG. Co. LTD, Japan), and recorded at various temperatures in an Ar atmosphere ($P_{O2} = 10^{-6}$ atm). The schematic diagram of the equipment is shown in Figure 1.

Prior to each experiment, 0.2 g of the prepared slag was placed in a Pt crucible, heated in the hot stage of CLSM, and held for full melting at 1600 °C under Ar gas ($P_{O2} = 10^{-6}$ atm) for 5 min. Then the molten slag sample was quenched at a cooling rate of 10 °C/min. The microstructure and elemental distribution of the quenched slag were analyzed through scanning electron microscopy (ZEISS EVO 18) equipped with energy-dispersive X-ray spectroscopy (Xmax50 from Oxford Instrument) (SEM–EDS). Considering that the quantity of quenched slags obtained in the CLSM experiment could not meet the requirement of XRD analysis, repeated experiments were carried out in a vertical tube furnace with 40 g slag in each test to detect the precipitated phases of quenched samples by XRD (TTRIII from Rigaku Corporation). Complementary SEM–EDS analysis for the samples obtained in the vertical tube furnace was also carried out to verify the results from the samples obtained in the CLSM experiment.

To investigate the effect of oxygen partial pressure on the phase chemistry in the CaO–SiO_2–FeO–P_2O_5 melt, an experiment was carried out in parallel throughout under air atmosphere ($P_{O2} = 0.21$ atm), that is, the molten slag was melted, held and quenched under air. The sample obtained in the experiment under air is thereafter labeled as "0#" slag.

Table II. Composition of Simulated Steel Slag (Wt Pct)

Slag No	CaO	SiO_2	FeO	P_2O_5	B_2O_3
1#	38.57	15.43	36	10	0
2#	37.14	14.86	36	10	2
3#	35.71	14.29	36	10	4
4#	34.29	13.71	36	10	6
5#	32.86	13.14	36	10	8

Table I. Technical Condition of Phosphorus Recovery of Simulated Steel Slag (Wt Pct)

| Researcher	Additive	Amount	Temperature	Slag System
Li et al.[15]	SiO_2	10 pct	1500 °C	CaO–SiO_2–FeO–Fe_2O_3–P_2O_5
Jiang et al.[16]	Al_2O_3	11 pct	1450 °C	CaO–SiO_2–MgO–MnO–FeO–P_2O_5–Al_2O_3
Lin et al.[17,18]	SiO_2; Al_2O_3; TiO_2	10; 15; 10 pct	1450 °C	CaO–SiO_2–Fe_2O_3–P_2O_5
Yu et al.[19]	$Al_2O_3/TiO_2/Na_2O = 15:4:3$	30 pct	1550 °C	CaO–SiO_2–Al_2O_3–Fe_2O_3–P_2O_5
Li et al.[20]	Na_2O	14 pct	1400 °C	CaO–SiO_2–Fe_tO–P_2O_5
Chen et al.[21]	MgO	9.8 pct	1640 °C	CaO–SiO_2–MgO–MnO–FeO–P_2O_5
Zhang et al.[22]	Al_2O_3; TiO_2	11; 10 pct	1350 °C	CaO–SiO_2–MgO–MnO–Fe_tO–P_2O_5
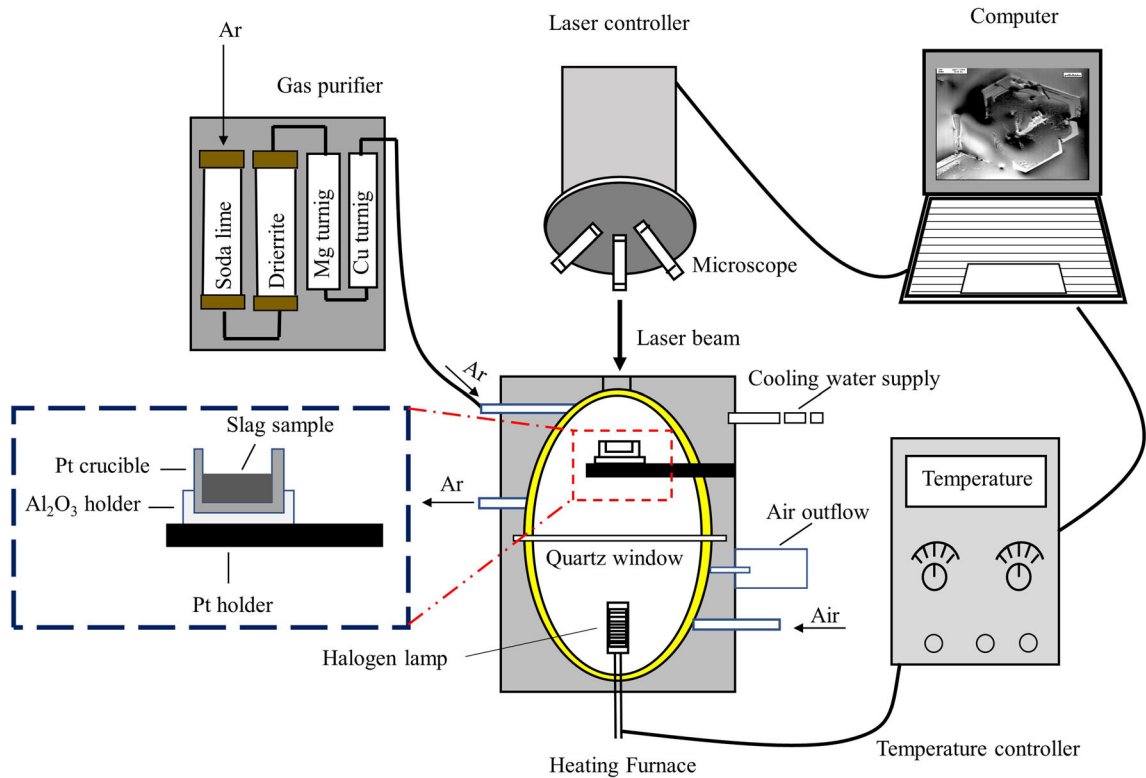
Fig. 1—Schematic diagram of CLSM equipment.
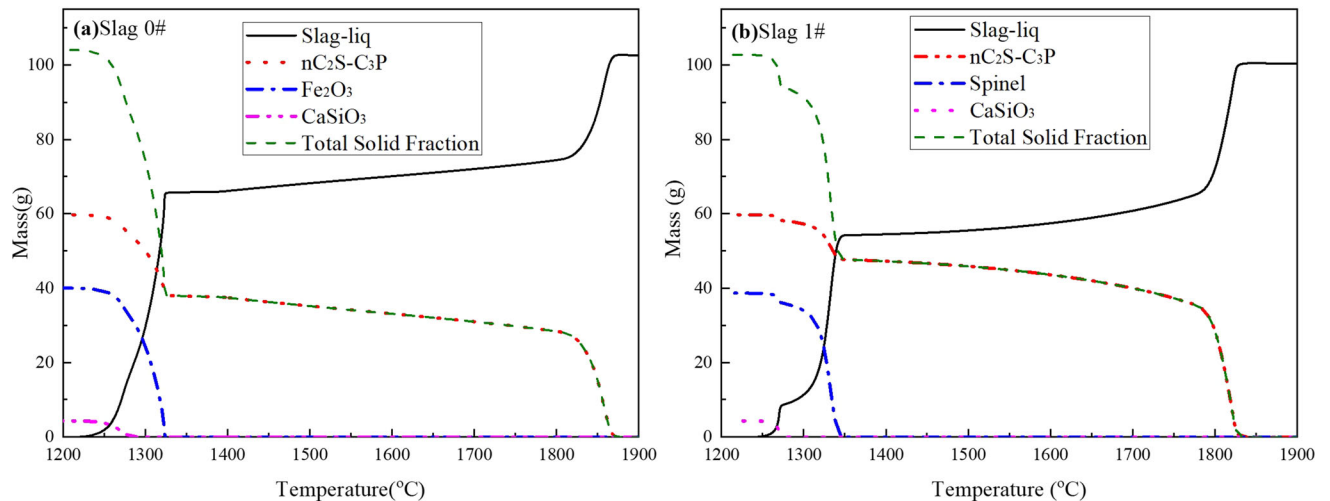
Fig. 2—Change in accumulated amount of different phases precipitated from slags with same composition under different oxygen pressures: (a) 0# (in air); (b) 1# (in high purity argon).

III. RESULTS

A. Thermodynamic Simulation of Precipitated Phases

To investigate the effect of oxygen partial pressure and B_2O_3 addition on the crystallization behavior of slags, FactSage 8.1 calculations were conducted to predict the precipitated phases of the slags studied. The calculations comprise two steps of molten slag equilibration and solidification in air ($P_{O2} = 0.21$ atm)

or Ar ($P_{O2} = 10^{-6}$ atm). Figures 2(a) and (b) show the change in accumulated amount of different phases precipitated in slags 0# ($P_{O2} = 0.21$ atm) and 1# ($P_{O2} = 10^{-6}$ atm). The effect of oxygen partial pressure on the precipitation of phosphorus-containing phase (nC_2S-C_3P) was found negligible. However, it completely changed the iron-containing phase from Fe_2O_3 in air ($P_{O2} = 0.21$ atm, Figure 2(a)) to spinel phase (Fe_3O_4) in argon ($P_{O2} = 10^{-6}$ atm, Figure 2(b)). Similar
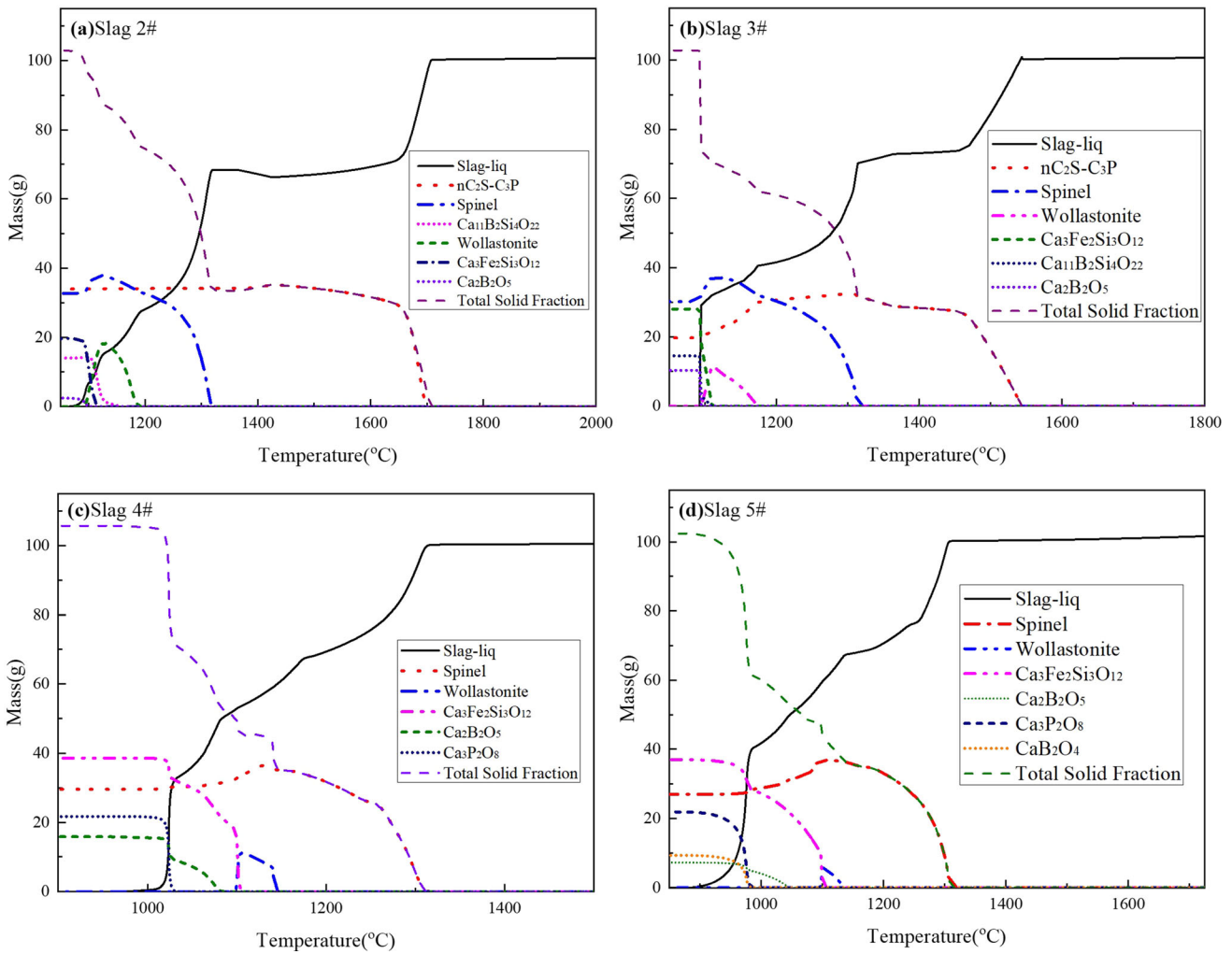
Fig. 3—Change in accumulated amount of different phases precipitated from slags in Ar atmosphere as a function of B_2O_3 addition: (a) 2#—2 pct B_2O_3; (b) 3#—4 pct B_2O_3; (c) 4#—6 pct B_2O_3; (d) 5#—8 pct B_2O_3.
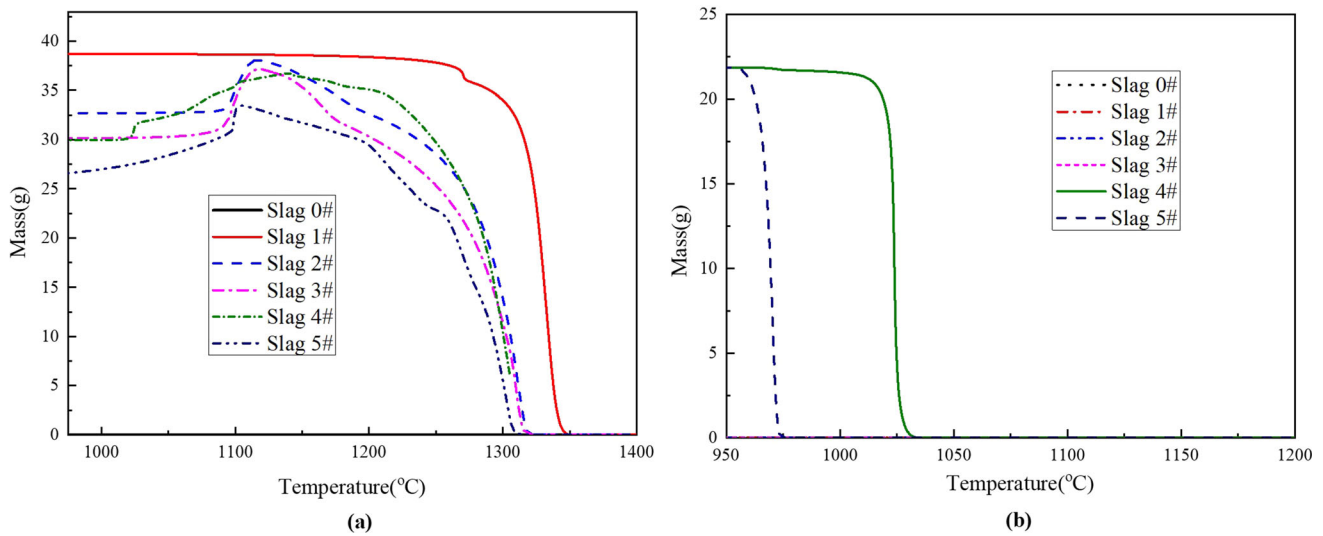

Fig. 4—Change in the accumulated amount of (a) Fe_3O_4 and (b) $Ca_3P_2O_8$ precipitated from different slags.

results were also found in previous papers for exposing the molten $CaO–SiO_2–FeO–MnO–Al_2O_3–MgO$ slag in Ar atmosphere.[38,39]

Figures 3(a) through (d) show the change in accumulated amount of different phases precipitated in slags 2#—5# in argon atmosphere ($P_{O2} = 10^{-6}$ atm) as a function of B_2O_3 addition. It was found that with the addition of B_2O_3, the primary phase changed from solid solution (nC_2S-C_3P) phase in slags 2# and 3# to spinel phase (Fe_3O_4) in slags 4# and 5#, and phosphorus-containing phases transformed from solid solution (nC_2S-C_3P) phase in slags 2# and 3# into $Ca_3P_2O_8$ in slags 4# and 5#. As can be seen, the temperature for the precipitation of primary phase and the solidus temperature, decreased with B_2O_3 addition from 2 to 8 pct. For example, primary phase precipitation occurred at 1706 °C (slag 2#—2 pct B_2O_3), 1544 °C (slag 3#—4 pct B_2O_3), 1311 °C (slag 4#—6 pct B_2O_3) and 1307 °C (slag 5#—8 pct B_2O_3) respectively. The reasons could be attributed to the fact that B_2O_3 works as a network former in the molten slag. It absorbs O^{2-} to form $[BO_3]$ triangles or $[BO_4]$ tetrahedral structural units, thus increasing the amount of network formers and the polymerization degree of the slag. Therefore, the diffusion of slag components in the slag is retarded, which is unfavorable to the precipitation of crystalline phases, leading to the weakening of slag melt crystallization.[40,41] It is interesting to note that with increasing B_2O_3 content from 2 pct (slag 2#) to 8 pct (slag 5#), the amount of precipitated spinel (Fe_3O_4) decreases slightly from 32.7 to 27.0 g, while that of $Ca_3Fe_2Si_3O_{12}$ increases from 19.6 to 38.7 g. This will be discussed in the Section III–C.

Figure 4 shows the change in the accumulated amount of (a) Fe_3O_4 (spinel) and (b) $Ca_3P_2O_8$ in synthetic slags. With changing oxygen partial pressure from 0.21 atm (slag 0#) to 10^{-6} atm (slag 1# to slag 5#), the content of spinel phase increased from 0 g (slag 0#) to 38.67 g (slag 1#) per 100 g slag. However, with increasing B_2O_3 addition from 2 pct (slag 2#) to 8 pct (slag 5#), the content of spinel phase (Fe_3O_4) gradually decreased from 32.71 g to 26.98 g per 100 g slag. As can be seen in Figures 3 and 4(b), $Ca_3P_2O_8$ does not exist in slag 2# (2 pct B_2O_3) and slag 3# (4 pct B_2O_3), but reaches 21.85 g in slag 4# (6 pct B_2O_3) and remains almost unchanged in slag 5# (8 pct B_2O_3), indicating that $Ca_3P_2O_8$ is saturated in the slag with 6 pct B_2O_3.

B. Crystallization Behaviors of the Slags with Varying B_2O_3 Additions

Figure 5 shows the crystallization behaviors of the synthetic slag 4# (6 pct B_2O_3) in argon ($P_{O2} = 10^{-6}$ atm) observed under CLSM at the cooling rate of 10 °C/min. For example, the morphology of the pre-melted slag at 1600 °C (Fig. 5(a)), the nucleus of the 1st phase crystal (C1) formed at 1243 °C (Figure 5(b)), and the frame of crystal formed at ~ 1216 °C (Figure 5(c)). With decreasing the temperature from 1243 °C to 1082 °C, the volume of the crystal nucleus increased gradually (Figures 5(b) through (e)). It is noticeable that the frame of the 2nd phase crystal (C2) formed at
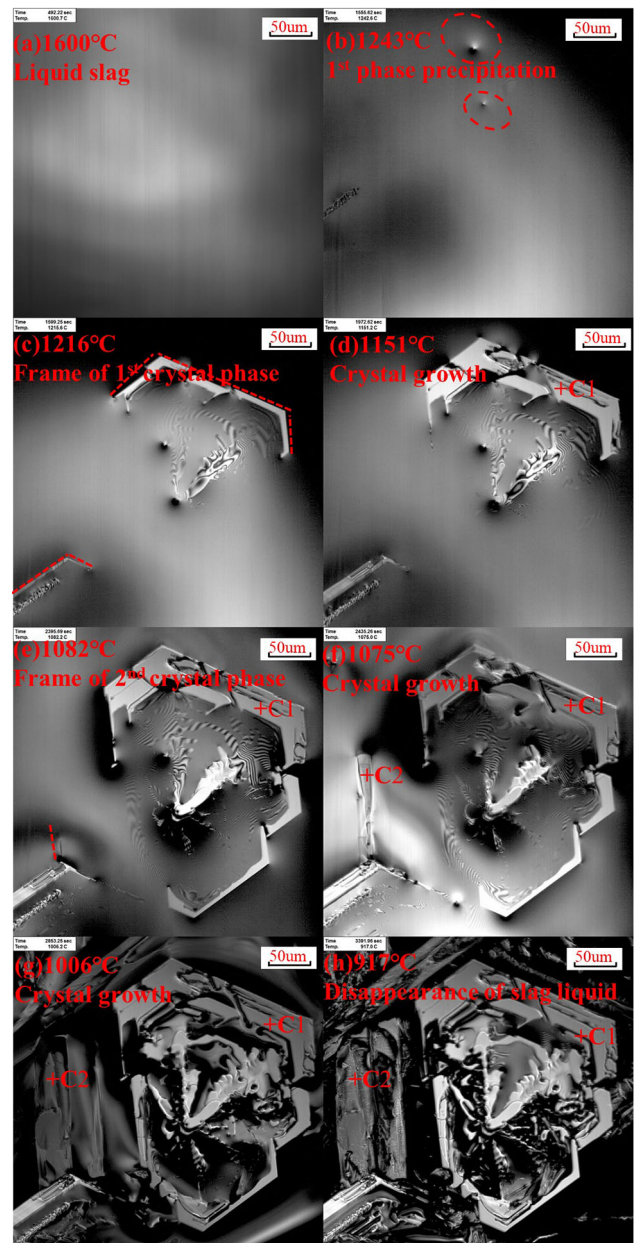

Fig. 5—Crystallization process of slag 4# in argon at the continuous cooling rate of 10 °C/min: (a) 1600 °C; (b) 1243 °C; (c) 1216 °C; (d) 1151 °C; (e) 1082 °C; (f) 1075 °C; (g) 1006 °C; and (h) 917 °C.

~ 1082 °C in Figure 5(e) and both phase crystals continuously grew in the temperature ranges from 1082 °C to 917 °C. Finally, the liquid slag appeared to have fully crystallized at 917 °C in Figure 5(h).

Figure 6 compares the CLSM morphology of the crystalline in the slag 4# at the continuous cooling rate of 10 °C/min with the corresponding SEM morphology, indicating good agreement between these two. As shown in Figure 6(b), mainly three phases in the slag 4# were observed, namely the lath-shaped phase (P1 and P2), white hexagonally faceted crystal (P3 and P4) and slag matrix (P5 and P6). It is noticeable that these white hexagonally faceted crystals were surrounded by the lath-shaped phase and slag matrix, indicating an early
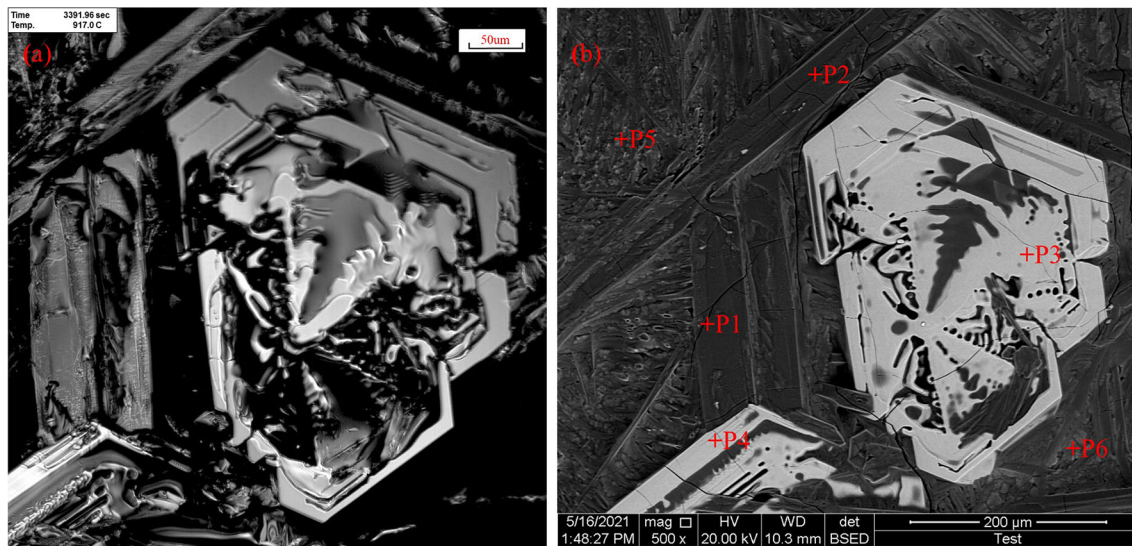
Fig. 6—Morphologies of the crystalline in the slag 4# at continuous cooling rate of 10 °C/min (a) CLSM image and (b) SEM image.

crystallization, in comparison to the lath-shaped phase and slag matrix. Moreover, the length of lath-shaped crystals was no more than 500 μm, while the diameter of these white crystals was approximately 200 μm. In order to determine the elementary distribution in different phases, EDS mapping analysis was employed and the corresponding results are presented in Figure 7. Phosphorus was mainly enriched in the lath-shaped phase, while Fe was mainly concentrated in the white hexagonally faceted phase. Moreover, Ca and Si were concentrated in the matrix phase. EDS spot analysis (Table III) indicated that the lath-shaped phase was close to $Ca_2PO_{4.8}$ (or Ca_2PO_4), while the white hexagonally faceted phase and slag matrix were approaching $Fe_3O_{3.9}$ (or $Fe_3O_{4.2}$) and $CaFe_{0.3}Si_{0.7}O_{2.1}$ (or $CaFe_{0.3}Si_{0.8}O_{2.1}$) respectively.

The crystallization behaviors observed by CLSM and precipitated phases analyzed by XRD and SEM–EDS were similar for other slags but not reproduced here for the brevity of the paper. However, the comparison of precipitated phases for slag 1# (without B_2O_3 addition) and slag 4# (6 pct B_2O_3) is summarized in Table IV. As shown in Table IV, a lath-shaped morphology as the 1st precipitated phase and a hexagonally faceted crystal as the 2nd precipitated phase for the slag 1# were observed to start precipitating at 1301 °C and 1264 °C, respectively, while it was the inverse of phase precipitation sequence for the slag 4#. Moreover, the potential formula of the hexagonally faceted phases for both slag 1# and slag 4# was close to magnetite phase (Fe_3O_4), while the lath-shaped phase was close to $Ca_7Si_{3.6}P_{2.5}O_{12}$ (or $Ca_7Si_{3.9}P_{2.4}O_{10.3}$) for slag 1# and $Ca_2PO_{4.8}$ (or Ca_2PO_4) for slag 4# respectively. The different phase precipitation sequence and potential formula of the precipitated phases for slags 1# and 4# could be attributed to factors such as undercooling,[42] slag composition[43] and enthalpy of mixing (so-called Jackson α factor[44]), which will be reported in a separate paper.

C. Phase Characterization

In order to explore the effect of oxygen partial pressure and B_2O_3 addition on the crystallization process of samples, the phases presented in the slags were characterized using XRD. Figures 8(a) through (f) show phases presented in the slag 0# to 5# at the continuous cooling rate of 10 °C/min. It should be pointed out that slag 0# was cooled in air (P_{O2} = 0.21 atm), while slags 1# to #5 were cooled in argon atmosphere (P_{O2} = 10^{-6} atm). As can be seen in Figure 8(a), it was shown clearly that three phases were detected in slag 0#, namely $Ca_2Fe_2O_5$, $Ca_7Si_2P_2O_{16}$ and Ca_2SiO_4. Fe existed in the form of calcium ferrite phase, while P was concentrated in the $Ca_7Si_2P_2O_{16}$ phase in the synthetic slag 0# (P_{O2} = 0.21 atm). However, with changing oxygen partial pressure from 0.21 atm (slag 0#) to 10^{-6} atm (slag 1#), the predominant iron-containing phase ($Ca_2Fe_2O_5$) transformed into magnetite phase (Fe_3O_4), as shown in Figure 8(b), while other phases remained the same as in the slag 0#. Compared with slag 1#, dicalcium silicate (Ca_2SiO_4) was not detected in slag 2#, while two new phases of $CaFeSi_2O_6$ and $Ca_{11}B_2Si_4O_{22}$ were found after adding 2 pct B_2O_3 as shown in Figure 8(c). As can be seen in Figure 8(d) for slag 3# containing 4 pct B_2O_3, the phosphorus-rich phase of calcium phosphate ($Ca_{10}P_6O_{25}$) was detected and the B-containing phase was identified as the calcium borate phase ($Ca_2B_2O_5$), rather than $Ca_{11}B_2Si_4O_{22}$. As for the slags with B_2O_3 addition of 6 pct (slag 4#) and 8 pct (slag 5#), calcium phosphate ($Ca_{10}P_6O_{25}$) remained the only phosphorus-rich phase, and the B-containing phase transformed from $Ca_2B_2O_5$ (Slag #3) to CaB_2O_4 (Slags 4# and 5#). In summary, with simultaneous change of oxygen partial pressure from 0.21 atm (in air) to 10^{-6} atm (in argon) and addition of B_2O_3 (6 pct) into the simulated steelmaking slag, phosphorus- and iron-containing phases precipitated in the form of Fe_3O_4 and $Ca_{10}P_6O_{25}$ respectively during the cooling process from 1600 °C to 900 °C.
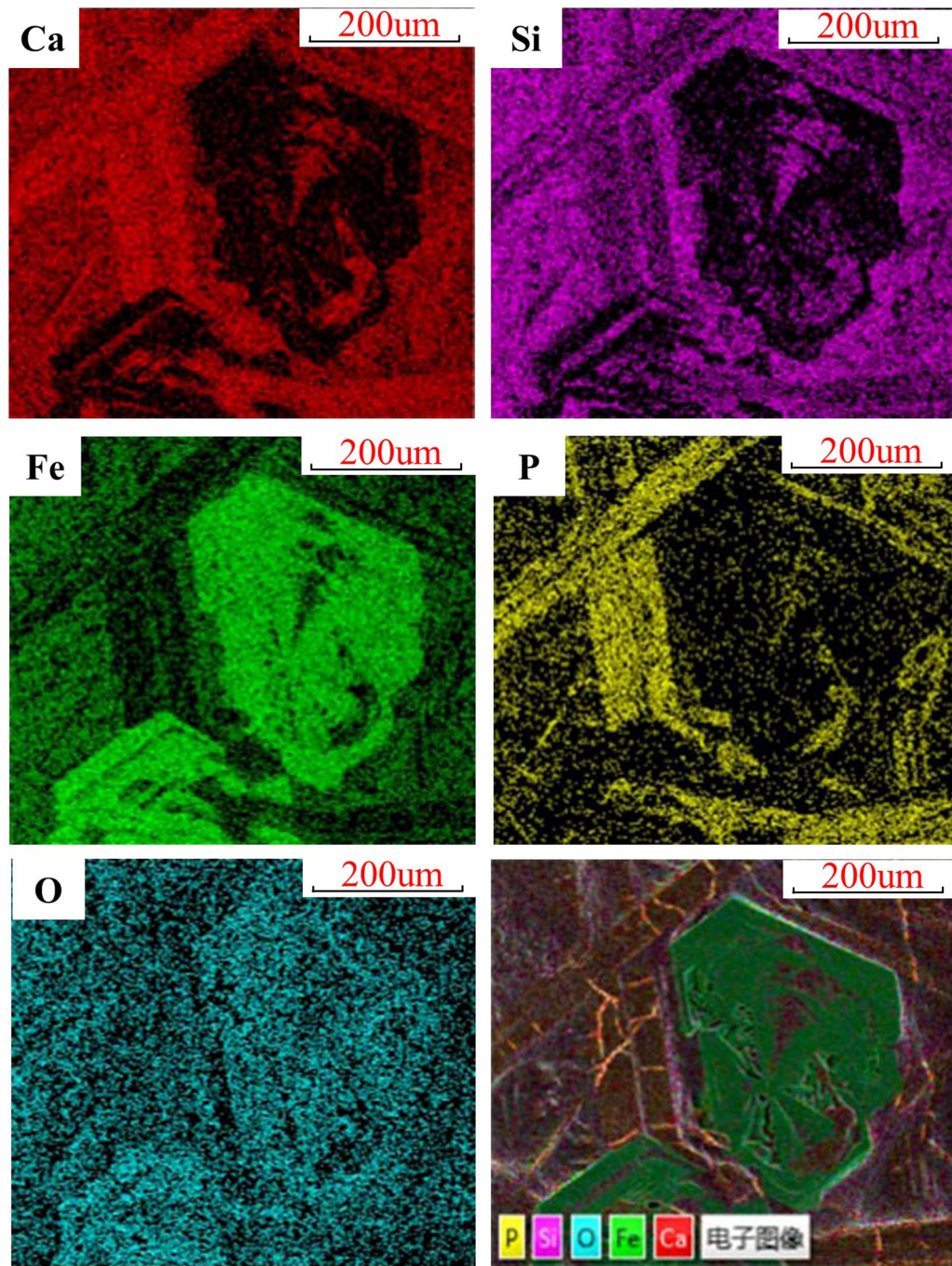
Fig. 7—EDS map scanning of slag 4# at the continuous cooling rate of 10 °C/min.

Table III. EDS Analysis of Different Phase Areas in the Slag 4# at the Continuous Cooling Rate of 10 °C/min, Corresponding to Fig. 6(b) (Wt Pct)

	Ca	Si	O	P	Fe	Potential Formula
Pt1	41.87	1.25	40.01	16.87	—	$Ca_2PO_{4.8}$
Pt2	44.28	2.43	35.74	17.55	—	Ca_2PO_4
Pt3	1.19	—	26.71	—	72.1	$Fe_3O_{3.9}$
Pt4	2.88	0.53	27.64	—	68.95	$Fe_3O_{4.2}$
Pt5	36.28	17.83	31.13	0.55	14.21	$CaFe_{0.3}Si_{0.7}O_{2.1}$
Pt6	35.03	18.53	29.59	—	16.85	$CaFe_{0.3}Si_{0.8}O_{2.1}$

— indicates that the elements involved have not been detected due to their relatively tiny amount in the phase area; low X-ray energy boron has not been listed in this table.

From SEM–EDS analysis (Figure 9; Table V), it is clear that the irregular white phase in Figure 9(a) is composed primarily of Ca, Fe and O, while the spinel type and/or dendritic white phases in Figures 9(b) through (f) are made up of Fe and O, with chemical formula approaching Fe_3O_4. It indicates that oxygen partial pressure is the key to the transformation of iron oxides in the CaO–SiO_2–FeO–P_2O_5 slags. In Figures 9(a) and (b), the round granular phase was primarily made up of Ca, Si, P and O, corresponding to the phosphate-containing phase of $Ca_7Si_2P_2O_{16}$, while the slag matrix was composed primarily of Ca, Si and O, corresponding to the dicalcium silicate ($2CaO \cdot SiO_2$). As can be seen from Figures 9(c) through (f), the dark lath-shaped or/and faceted morphology phase started to form in slag 3# (4 pct B_2O_3, Figure 9(d)) and enlarged with increasing B_2O_3 content, which could be attributed to the fact that B_2O_3 addition gave rise to a decrease in slag viscosity. As Ca, P and O were enriched in the abovementioned dark phase and the chemical formula was close to the phosphorus-rich phase of calcium phosphate ($Ca_{10}P_6O_{25}$), it is reasonable to conclude that B_2O_3 is an effective additive to extract phosphate from steelmaking slag.

By comparing the integrated intensities of the diffraction peaks from each of the known phases, the weight fractions of phosphorus- and iron-containing phases in the slags were semi-quantitatively determined and listed in Table VI. As seen in Table VI, by changing the oxygen partial pressure from 0.21 atm (slag 0#) to 10^{-6} atm (slag 1#), the amount of magnetic phase greatly increased from 0 to 38 g while that of the solid solution phase ($Ca_7Si_2P_2O_{16}$) varied slightly. With B_2O_3 addition from 2 pct (slag 2#) to 8 pct (slag 5#), the amount of solid solution ($Ca_7Si_2P_2O_{16}$) phase in argon ($P_{O_2} = 10^{-6}$ atm) decreased from 29 to 0 g, while that of calcium phosphate ($Ca_{10}P_6O_{25}$) first increased and then decreased, with the maximum of 28 g per 100 g slag at 6 pct B_2O_3 addition (slag 4#). Moreover, the quantity of spinel (Fe_3O_4) decreases slightly while that of $CaFeSi_2O_6$ increases with increasing B_2O_3 content, which agree well with the results of thermodynamic calculation in this paper. The reasons could be attributed to the fact that high melting point substances could be transformed into low melting point phases by adding B_2O_3 into slags.[33,45,46] In this case, it could be deduced that a small amount of low melting point phase of $CaFeSi_2O_6$ (1217 °C) was generated through the reaction (1).

$$CaO + FeO + 2SiO_2 = CaFeSi_2O_6 \qquad [1]$$
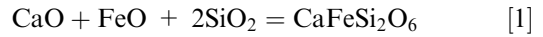
$$\Delta G = -121874.7 + 21.11T \text{ [J/mol]}$$

By combining the crystallization behavior observed by CLSM, the microstructure analyzed by SEM–EDS and the phases present in the slags characterized by XRD, for the slag 1#, the 1st and 2nd phases observed at 1301 °C and ~ 1264 °C can be considered solid solution ($Ca_7Si_2P_2O_{16}$) and magnetite (Fe_3O_4). This agrees with the calculation result by FactSage 8.1 (Figure 2(b)). Similarly, it could be concluded that the 1st and 2nd phases in slag 4# observed at 1243 °C in Figure 5(b) and ~ 1082 °C in Figure 5(e) are Fe_3O_4 and $Ca_{10}P_6O_{25}$ respectively.

IV. DISCUSSION

A. *Influence of Oxygen Partial Pressure*

Figure 10, the phase diagram of CaO–SiO_2–FeO–P_2O_5 slag, demonstrates that the presence of iron oxide species in the solid product depends on oxygen partial pressure. Wustite (FeO) in the slag is oxidized to magnetite under the oxygen pressure of 10^{-6} atm or to hematite under the oxygen pressure of 0.21 atm. It should be pointed out that the precipitated phases of the slag that have been described by the phase diagrams in Figure 10 are for equilibrium conditions, which can be approximated by slow cooling. However, the relatively large cooling rate of 10 °C/min is applied in this study, causing the deviation from equilibria between the slag samples and the gas atmosphere. Fortunately, the main precipitated phases, such as magnetite (Fe_3O_4), $Ca_7Si_2P_2O_{16}$ and Ca_2SiO_4, predicted by phase diagrams in Figure 10 and characterized by the XRD pattern (in Figure 8(b)) keep the same. For industry applications, in order to recover iron from the slag in the form of magnetite (Fe_3O_4) by magnetic separation, the molten slag should be solidified at a slow cooling rate from about 1350 °C as illustrated in Figure 10 to give Fe_3O_4 enough time to precipitate. In addition, for the air-treated slag (slag 0#), Fe^{2+} in the slag (FeO) is oxidized to Fe^{3+} (Fe_2O_3) according to Reaction (2) as shown in Figure 10. However, the XRD pattern (Figure 8(a)) for the air-treated slag (slag 0#) demonstrates the presence of the main iron-containing

Table IV. Comparison of Precipitated Phases for Slag 1# and Slag 4#

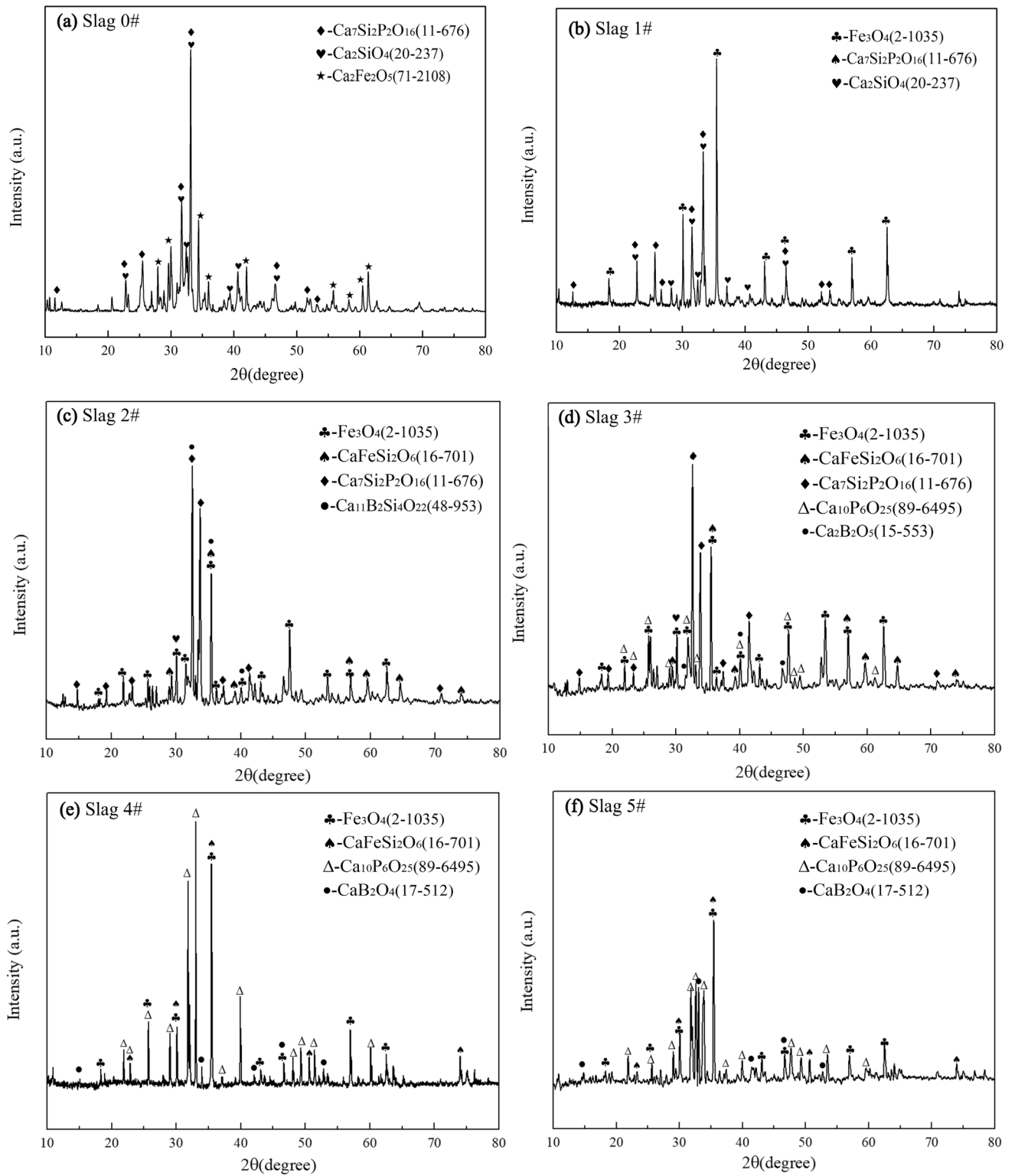|	Slag 1#		Slag 4#	
	1st Crystal Phase	2nd Crystal Phase	1st Crystal Phase	2nd Crystal Phase
Morphology	lath-shaped	hexagonally faceted	hexagonally faceted	lath-shaped
Temperature of starting precipitation	1301 °C	1264 °C	1243 °C	1082 °C
Potential Formula	$Ca_7Si_{3.6}P_{2.5}O_{12}$ (or $Ca_7Si_{3.9}P_{2.4}O_{10.3}$)	$Fe_3O_{4.0}$ (or $Fe_3O_{3.7}$)	$Fe_3O_{3.9}$ (or $Fe_3O_{4.2}$)	$Ca_2PO_{4.8}$ (or Ca_2PO_4)

Fig. 8—X-ray diffraction patterns of samples at the continuous cooling rate of 10 °C/min: (*a*) Slag 0#; (*b*) Slag 1#; (*c*) Slag 2#; (*d*) Slag 3#; (*e*) Slag 4#; (*f*) Slag 5#.
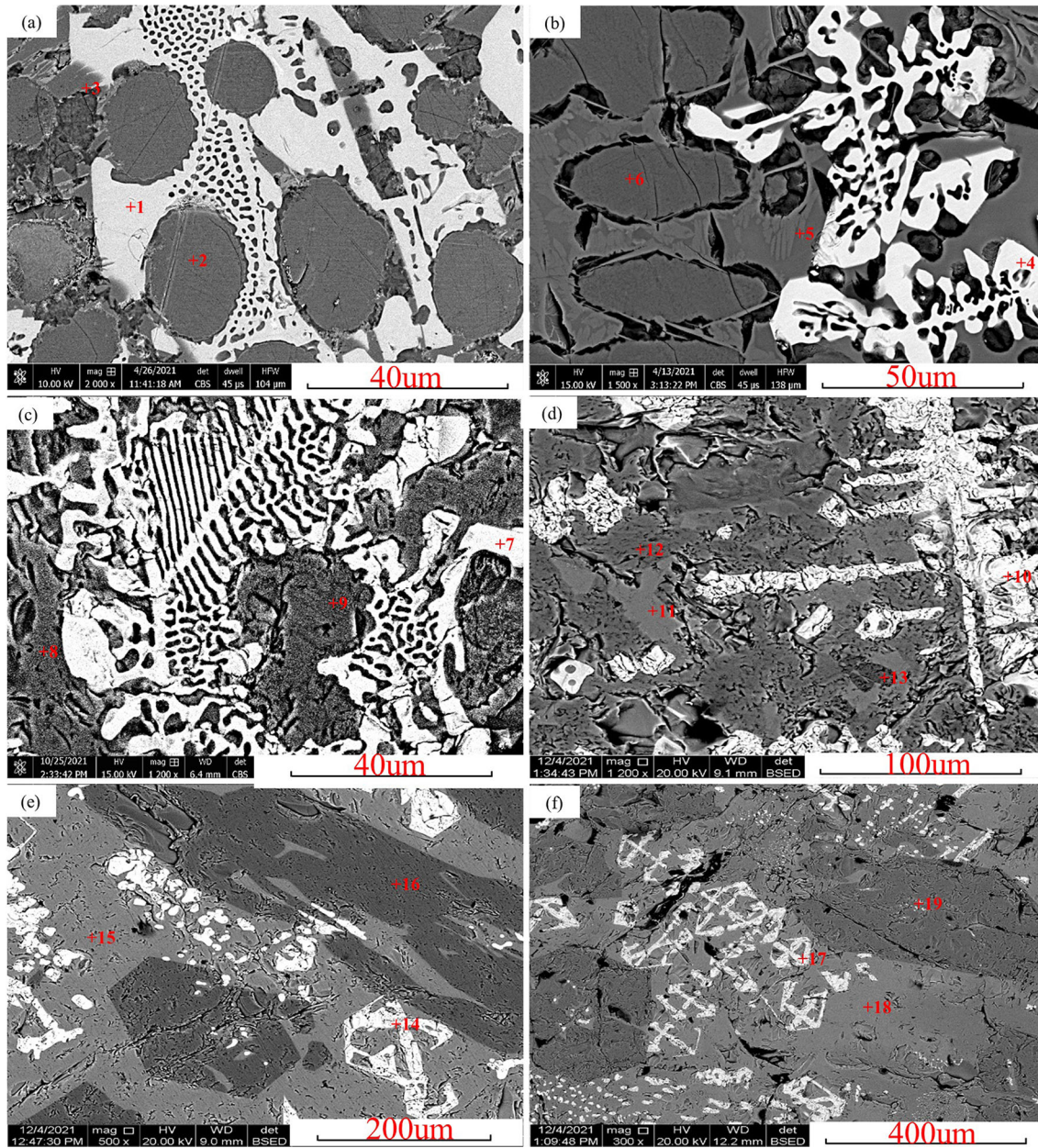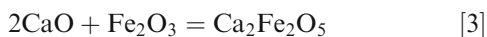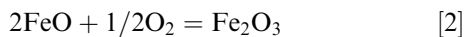
Fig. 9—SEM results of six samples: (*a*) Slag 0#; (*b*) Slag 1#; (*c*) Slag 2#; (*d*) Slag 3#; (*e*) Slag 4#; (*f*) Slag 5#. Slag 0# was cooled in air (P_{O2} = 0.21 atm) while slags 1# to 5# were cooled in argon (P_{O2} = 10^{-6} atm).

phase $Ca_2Fe_2O_5$ rather than Fe_2O_3, implying that the formed hematite further stabilizes the free lime by forming $Ca_2Fe_2O_5$ according to Reaction (3).

$$2FeO + 1/2O_2 = Fe_2O_3 \qquad [2]$$

$$2CaO + Fe_2O_3 = Ca_2Fe_2O_5 \qquad [3]$$

The deviation of the prediction and experimental result could be attributed to different conditions for the calculations and laboratory experiments, that is, the experimental conditions might be far from the equilibrium state in the thermodynamic prediction. In the actual crystallization process, reactions are affected by

various kinetic factors such as the reaction time, the reaction area of the system studied, *etc*. It is evidenced that the $Ca_2Fe_2O_5$ phase is the dominant iron-containing phase in the steelmaking slag under high oxygen partial pressure (*e.g.* in the air).[21,38,39]

In contrast, for the slags treated in Ar atmosphere (P_{O2} = 10^{-6} atm), the oxidizing processes in the molten slag can be expressed by reaction (4):

$$6FeO + O_2 = 2Fe_3O_4 \qquad [4]$$
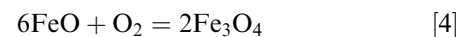
As seen in Figure 8(b), spinel (Fe_3O_4) is the stable solid iron oxide under Ar atmosphere (P_{O2} = 10^{-6} atm) in the present study. This is also supported by the fact that the magnetite (Fe_3O_4) primary phase field

Slag No	Position	Phases	Ca	Si	O	P	Fe	Potential Formula
0#	Pt1	Fe-rich	20.61	5	20.66	—	53.73	$Ca_2Fe_{3.7}O_{4.8}$
	Pt2	Matrix	50.9	16.32	31.67	—	1.02	$Ca_2Si_{0.91}O_{3.1}$
	Pt3	P-rich	43.26	20.06	22.33	14.35	—	$Ca_7Si_{4.67}P_{2.98}O_{9.1}$
1#	Pt4	Fe-rich	3.32	—	26.35	—	70.33	$Fe_3O_{3.93}$
	Pt5	Matrix	50.04	15.9	33.61	—	0.45	$Ca_2Si_{0.91}O_{3.4}$
	Pt6	P-rich	44.82	19.77	23.06	12.35	—	$Ca_7Si_{4.44}P_{2.49}O_9$
2#	Pt7	Fe-rich	—	—	28.69	—	77.31	$Fe_3O_{3.89}$
	Pt8	Matrix	50	15.11	33.61	—	—	$Ca_2Si_{0.86}O_{3.36}$
	Pt9	P-rich	40.26	18.34	25.78	15.39	—	$Ca_7Si_{4.57}P_{3.57}O_{11.2}$
3#	Pt10	Fe-rich	—	—	28.4	—	71.6	$Fe_3O_{4.16}$
	Pt11	Matrix	19.76	11.67	44.97	—	23.6	$CaFe_{0.85}Si_{0.84}O_{5.68}$
	Pt12	P-rich	40.49	18.34	25.78	15.59	—	$Ca_7Si_{4.5}P_{3.47}O_{11.2}$
	Pt13	P-rich	40.53	—	46.25	13.22	—	$Ca_3P_{1.31}O_{8.58}$
4#	Pt14	Fe-rich	—	—	29.11	—	70.89	$Fe_3O_{4.3}$
	Pt15	Matrix	41.78	16.98	27.5	1.34	12.4	$CaFe_{0.21}Si_{0.58}O_{1.64}$
	Pt16	P-rich	49.37	0.06	34.55	16.02	—	$Ca_3P_{1.25}O_{5.24}$
5#	Pt17	Fe-rich	—	—	32.6	—	67.4	$Fe_3O_{5.1}$
	Pt18	Matrix	20.94	11.75	46.59	—	20.72	$CaFe_{0.71}Si_{0.81}O_{5.6}$
	Pt19	P-rich	36.64	—	46.84	16.52	—	$Ca_3P_{1.8}O_{9.56}$

— indicates that the elements involved have not been detected due to their relatively tiny amount in the phase area; low X-ray energy boron has not been listed in this table.

has replaced the hematite (Fe_2O_3) primary phase field as the dominant feature of the iron oxide-rich corner of the $CaO–FeO_x–SiO_2$ diagram at the effective oxygen partial pressure between $10^{-3.9}$ and $10^{-3.7}$ atm.[21]

To summarize, oxygen partial pressure is the key to oxidation state of iron oxides in the $CaO–SiO_2–FeO–P_2O_5$ melt. In air, FeO is oxidized to Fe_2O_3, which combines with free lime in the slag to form $Ca_2Fe_2O_5$, while under an atmosphere with low oxygen partial pressure, FeO is oxidized to Fe_3O_4.

B. Influence of B_2O_3 Addition

Figure 11 shows Gibbs free energy change of relevant reactions as a function of temperature calculated by FactSage 8.1. It clearly shows that the descending order for component formation is $3CaO \cdot P_2O_5$ (reaction (5)) > $2CaO \cdot B_2O_3$ (Reaction (6)) > $2CaO \cdot SiO_2$ (Reaction (7)). The preferential formation of $2CaO \cdot B_2O_3$ rather than $2CaO \cdot SiO_2$ inhibits the generation of solid solution $nCaO \cdot SiO_2$-$3CaO \cdot P_2O_5$ in the slag. It is in accord with the phase precipitation sequence observed by CLSM in Figure 5 and the precipitated phases characterized by XRD in Figure 8. The reasons could be attributed to not only the activity of CaO in the slag becomes small with the B_2O_3 addition based on the thermodynamic calculation and molecular theory for slag structure proposed by H. Schenck,[47,48] but also the reaction mechanism in the molten B_2O_3 modification process demonstrated by the theory of bond parameter function.[49]

It should be pointed out that B_2O_3 addition to the molten slag causes two contradictory effects on nucleation and growth of the magnetic spinel phase (Fe_3O_4). First, B_2O_3 can lower the melting temperature and viscosity of slag by forming a series of low melting compounds, which is beneficial for the migration of ions

Table VI. Weight Fraction (Pct) of Phosphorus- and Iron-Containing Phases in the Slags

Minerals	0#	1#	2#	3#	4#	5#
Magnetite (Fe_3O_4)	0	38	34	33	31	30
$CaFeSi_2O_6$	0	0	18	22	25	28
Solid Solution ($Ca_7Si_2P_2O_{16}$)	41	43	29	18	0	0
Calcium Phosphate ($Ca_{10}P_6O_{25}$)	0	0	0	12	28	25

and molecules in the molten slag, resulting in the growth of Fe_3O_4 crystals. Secondly, B_2O_3 addition can also weaken the crystallization ability of Fe_3O_4 phase by increased component diffusion resistance originating from the increased polymerization degree of slag melts, resulting in the small nucleation rate of Fe_3O_4 phase. In fact, the intensity of characteristic peaks of Fe_3O_4 phase slightly decreased with the increase of B_2O_3 addition from 2 to 8 pct as obviously illustrates in Figures 8(c) through (f). In view of these two aspects, it seems that B_2O_3 plays a little bit antagonism effect on the precipitation of Fe_3O_4 phase from the molten synthetic slags under Ar atmosphere.

Combining the results of thermodynamic calculation, crystallization behavior observed through CLSM, microstructure analyzed by SEM–EDS and the phases present in the slags characterized by XRD, reactions during slag modification with B_2O_3 addition can be expressed in Eqs. [5] through [7], and the schematic diagram of the molten slag modification by atmosphere control and B_2O_3 addition could be illustrated in Figure 12. Compared with the previous processes in Table I, the new process has two advantages: the lower energy consumption and smaller amount of additive B_2O_3 required. First, B_2O_3 was added into molten steelmaking slag during the slag tapping process, and
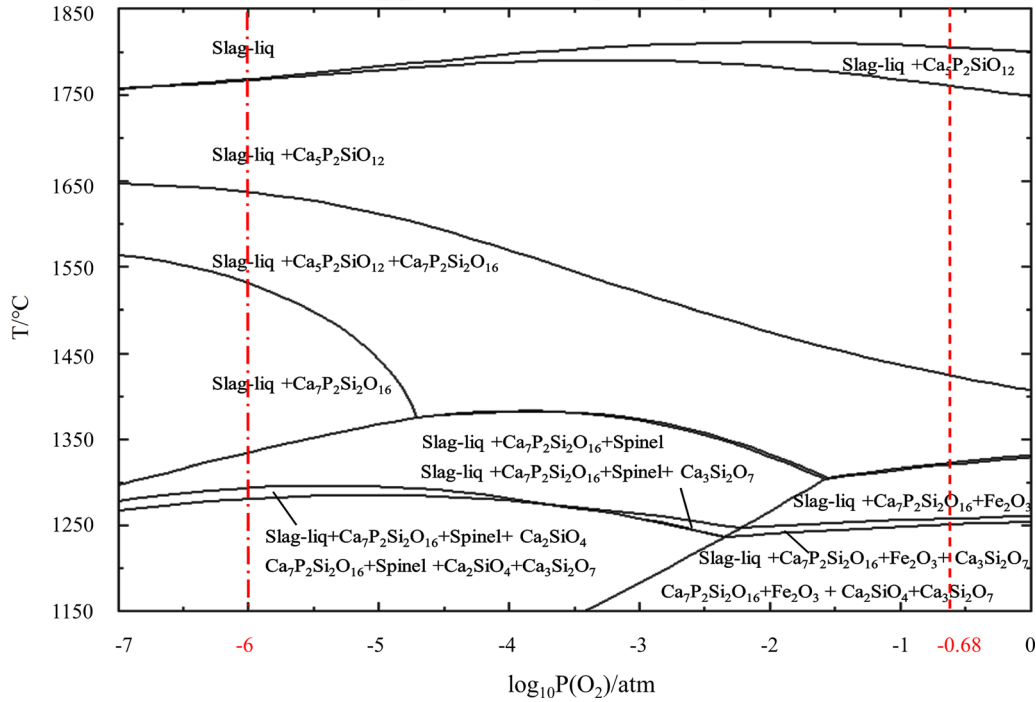
Fig. 10—Phase diagram of CaO–SiO$_2$–FeO–P$_2$O$_5$ system with the dotted line and dot-dash line corresponding to oxygen partial pressure in air and argon, respectively.
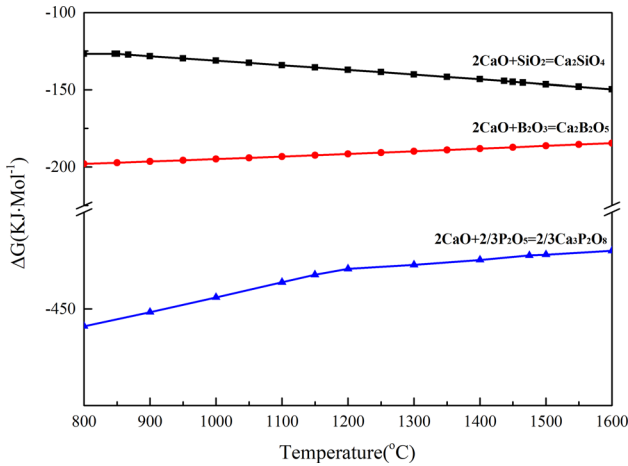

Fig. 11—Gibbs free energy change of relevant reactions calculated by FactSage 8.1.

the specific heat capacity for steelmaking slag is about 800 J/(kg·°C).[50–53] Therefore, the new process uses at least 355 kWh/t sensible heat of molten steelmaking slag and meanwhile avoids at least 290 kWh/t reheating for the modification in previous processes in Table I. Second, the B$_2$O$_3$ amount in the new process is smaller than that in the previous processes in Table I.

$$3CaO + P_2O_5 = Ca_3P_2O_8 \qquad [5]$$

$$CaO + B_2O_3 = CaB_2O_4 \qquad [6]$$

$$2CaO + SiO_2 = Ca_2SiO_4 \qquad [7]$$
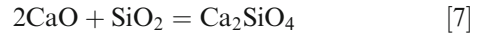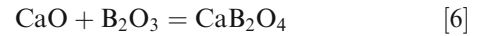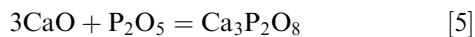
The current study confirms that Fe and P in synthetic steelmaking slags can be concentrated in the form of magnetite (Fe$_3$O$_4$) and calcium phosphate (Ca$_{10}$P$_6$O$_{25}$) phases by oxygen partial pressure control and B$_2$O$_3$ addition. Subsequently, the optimum temperature range for the crystallization of Fe$_3$O$_4$ and Ca$_{10}$P$_6$O$_{25}$ phases was obtained as (1055 $\pm$ 25)°C by both theoretical calculation and experiment.[54] In order to separate phosphorus and iron phases from the quenched slags, a wet magnetic separator (XCGQ-500 with the magnetic field intensity of 3.0 KOe was firstly employed to separate magnetite phase from the slag bulk. Subsequently, the flotation machine (XFD-0.75L) was used to separate the phosphorus-enriched phase from the non-magnetic part of magnetic separation. Using a combination of magnetic separation and flotation, the concentrates were obtained with Fe$_3$O$_4$ and P$_2$O$_5$ content of 92.84 and 37.66 pct, respectively, corresponding to the recovery ratios of 85.8 pct for iron and 91.3 pct for phosphorus. The recycled materials of iron and phosphorus concentrates could be considered as a potential source for ferrous feedstock and phosphate fertilizer, respectively.[55]
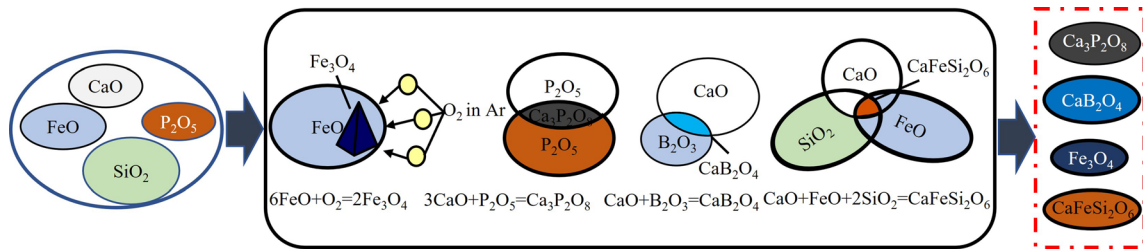
Fig. 12—Schematic diagram of the slag modification.

V. CONCLUSION

In this study, the effect of oxygen partial pressure and B_2O_3 addition on the crystallization behavior of iron- and phosphorus-containing phases in a CaO–SiO_2–FeO–P_2O_5 melt has been investigated. The main conclusions can be summarized as follows:

(1) Recovery of iron and phosphorus from the CaO–SiO_2–FeO–P_2O_5 slag can be effectively achieved through oxygen partial pressure control and B_2O_3 addition, through the precipitation in the melt of magnetite (Fe_3O_4) and calcium phosphate ($Ca_{10}P_6O_{25}$) phases, respectively.
(2) Oxygen partial pressure is the key to the precipitation of iron oxides in the CaO–SiO_2–FeO–P_2O_5 slags. Both thermodynamic calculation and experimental results indicated that with decreasing oxygen partial pressure from 0.21 to 10^{-6} atm, the precipitated iron oxides transformed from ferric oxide (Fe_2O_3) to magnetite (Fe_3O_4).
(3) Both thermodynamic calculation and experimental result indicated that by adding B_2O_3 from 2 to 8 pct, the amount of calcium phosphate ($Ca_{10}P_6O_{25}$) first increased and then decreased, with the maximum occurring at 6 pct B_2O_3.

CONFLICT OF INTEREST

The authors declare no potential conflict of interest.

REFERENCES

1. J.F. Li, C.X. Luo, M.K. Sun, W.G. Shen, B. Cao, and X.L. Li: *Key Eng. Mater.*, 2014, vol. 3019, pp. 98–102.
2. L. Lin, Y.Q. Liu, J.G. Zhi, S. He, X. Li, Z.X. Hou, and L.Q. Zhang: *Ironmak. Steelmak.*, 2021, vol. 48, pp. 334–42.
3. X.M. Yang, M. Zhang, G.M. Chai, J.Y. Li, Q. Liang, and J. Zhang: *Ironmak. Steelmak.*, 2016, vol. 43, pp. 663–87.
4. Z.W. Wang, B. Liang, and J.R. Zhang: *Appl. Mech. Mater.*, 2014, vol. 3013, pp. 1501–05.
5. M.Y. Kazuyo, K. Hironari, and N. Tetsuya: *IJSJ Int.*, 2010, vol. 50, pp. 65–70.
6. X. Lan, J.T. Gao, Y. Du, and Z.C. Guo: *J. Alloys Compd.*, 2018, vol. 731, pp. 873–70.
7. J.T. Gao, Y. Li, G.L. Xu, F.Q. Wang, Y. Lu, and Z.C. Guo: *ISIJ Int.*, 2017, vol. 57, pp. 587–89.
8. J.T. Gao, L. Guo, Y.W. Zhong, H.R. Ren, and Z.C. Guo: *Int. J. Miner. Metall. Mater.*, 2016, vol. 23, pp. 743–50.
9. Y.Y. Zhang, Q.G. Xue, G. Wang, and J.S. Wang: *ISIJ Int.*, 2018, vol. 58, p. 2219.
10. M. Sugata, T. Sugiyama, and S. Kondo: *ISIJ Int.*, 1974, vol. 14, pp. 88–95.
11. S. Takeuchi, N. Sano, and Y. Matsushita. *Tetsu-to-Hagane´*, **1980**, vol.66, pp. 2050–57.
12. H.M. Xue, J. Li, Y.J. Xia, Y. Wan, L.J. Chen, and C.J. Lv: *Metals*, 2021, vol. 11, p. 216.
13. J.M. Gonzalez, C.J. Penn, and S.J. Livingston: *Water*, 2020, vol. 12, p. 1953.
14. G.F. Ye, J. Yang, R.H. Zhang, W.K. Yang, and H. Sun: *Int. J. Miner. Metall. Mater.*, 2021, vol. 28, pp. 66–75.
15. J.Y. Li, M. Zhang, M. Guo, and X.M. Yang: *Int. J. Miner. Metall. Mater.*, 2016, vol. 23, pp. 520–33.
16. L. Jiang, J. Diao, X.M. Yan, B. Xie, Y. Ren, T. Zhang, and G.Z. Fan: *ISIJ Int.*, 2015, vol. 55, pp. 564–69.
17. L. Lin, Y.P. Bao, M. Wang, W. Jiang, and H.M. Zhou: *J. Iron Steel Res. Int.*, 2014, vol. 21, pp. 496–502.
18. L. Lin, Y.P. Bao, and M. Wang: *ISIJ Int.*, 2014, vol. 54, pp. 2746–53.
19. K. Yu, Y.L. Zhang, F.S. Li, and M. Gao: *J. Iron Steel Res. Int.*, 2018, vol. 26, pp. 796–805.
20. G.Q. Li, C.Y. Zhu, Y.J. Li, X.Y. Huang, and M. Chen: *Steel Res. Int.*, 2013, vol. 84, pp. 687–94.
21. G.J. Chen and S.P. He: *Ironmak. Steelmak.*, 2014, vol. 42, pp. 433–38.
22. Y.L. Zhang, M. Guo, F.S. Li, and Y. Ke: *Arch. Metall. Mater*, 2018, vol. 63, pp. 1769–83.
23. J.Y. Li, M. Zhang, M. Guo, and X.M. Yang: *Metall. Mater. Trans. B*, 2014, vol. 45B, pp. 1666–82.
24. J. Ma, W. Li, G.Q. Fu, and M.Y. Zhu: *J. Sustain. Metall*, 2021, vol. 7, pp. 1190–99.
25. H.M. Wang, T.W. Zhang, H. Zhu, G.R. Li, Y.Q. Yan, and J.H. Wang: *ISIJ Int.*, 2011, vol. 51, pp. 702–06.
26. M. Nakamoto, T. Tanaka, L. Holappa, and M. Hämäläinen: *ISIJ Int.*, 2007, vol. 47, pp. 211–16.
27. S. Ren, J.L. Zhang, L.S. Wu, W.J. Liu, Y.N. Bai, X.D. Xing, and D.W. Kong: *ISIJ Int.*, 2012, vol. 52, pp. 984–91.
28. Y. Shi, Y.G. Wei, S.W. Zhou, B. Li, Y.D. Yang, and H. Wang: *J. Alloys Compd.*, 2020, vol. 822, 153478.
29. A.A. Babenko, R.R. Shartdinov, A.G. Upolovnikova, A.N. Smetannikov, and V.S. Gulyakov: *Izvestiya VUZ. Chernaya Metallurgiya*, 2019, vol. 62, pp. 769–73.
30. P. Zhang, J.H. Liu, Z. Wang, G. Qian, and W. Ma: *Metall Mater Trans B*, 2019, vol. 50B, pp. 304–11.
31. J. Qi, C. Liu, and M. Jiang: *ISIJ Int.*, 2018, vol. 58, pp. 186–93.

32. Y. Sun, J. Liao, K. Zheng, X.D. Wang, and Z.T. Zhang: *JOM*, 2014, vol. 66, pp. 2168–75.
33. W.L. Wang, J.Y. Chen, J. Yu, L.J. Zhou, S.F. Dai, and W.G. Tian: *Waste Management*, 2020, vol. 111, pp. 34–40.
34. L.J. Zhou, W.L. Wang, B.X. Lu, G.H. Wen, and J. Yang: *Metall. Mater. Int.*, 2015, vol. 21, pp. 126–33.
35. H. Matsuura, M. Kurashige, M. Naka, and F. Tsukihashi: *ISIJ Int.*, 2018, vol. 49, pp. 1283–89.
36. S.Y. Cheng, M. Shevchenko, P.C. Hayes, and E. Jak: *Metall. Mater. Trans. B*, 2021, vol. 52B, pp. 1891–1914.
37. J. Chen, M. Shevchenko, P.C. Hayes, and E. Jak: *ISIJ Int.*, 2019, vol. 59, pp. 805–09.
38. J.C. Li, D. Bhattacharjee, X.J. Hu, D.W. Zhang, S. Sridhar, and Z.S. Li: *Metall. Mater. Trans. B*, 2019, vol. 50B, pp. 1931–48.
39. J.C. Li, D. Bhattacharjee, X.J. Hu, D.W. Zhang, S. Sridhar, and Z.S. Li: *Metall. Mater. Trans. B*, 2019, vol. 50B, pp. 1023–34.
40. Y. Huang, C. B. Shi, X. X. Wan, J. L. Li, D. L. Zheng, and J. Li: *J. Iron Steel Res. Int*, **2021**, pp. 1–11.
41. W.L. Konijnendijk and J.M. Stevels: *J Non-Cryst Solids*, 1975, vol. 18, pp. 307–31.
42. X.F. Lei and X.X. Xue: *Trans. Nonferrous Met. Soc. China*, 2010, vol. 20, pp. 2294–98.
43. Y.B. Zong, D.Q. Cang, Y.P. Zhen, Y. Li, and H. Bai: *Trans. Nonferrous Met. Soc. China*, 2009, vol. 19, pp. 834–39.
44. G. Chen, J. Chen, J.H. Peng, and R.D. Wan: *Trans. Nonferrous Met. Soc. China*, 2010, vol. 20, pp. 198–204.
45. D.U. Tulyaganov, S. Agathopoulos, J.M. Ventura, M.A. Karakassides, O. Fabrichnaya, and J.M.F. Ferreira: *J. Eur. Ceram. Soc*, 2006, vol. 26, pp. 1463–71.
46. C.F. Yang and C.M. Cheng: *Ceram. Int*, 1999, vol. 25, pp. 383–87.
47. V. Shatokha, A. Semykina, J. Nakano, and S. Seetharaman: *J. Min. Metall. Sect. B*, 2013, vol. 49, pp. 169–74.
48. X.H. Huang: *Metallurgy Principle for Iron and Steel*, 3rd ed. Metallurgical Industry Press, Beijing, 2013.
49. H.L. Fan, H.M. Duan, K. Tan, Y.K. Li, D.F. Chen, M.J. Long, and T. Liu: *JOM*, 2017, vol. 69, pp. 1914–19.
50. H. Agalit, N. Zari, and M. Maaroufi: *Sol. Energy Mater. Sol. Cells*, 2017, vol. 173, pp. 168–76.
51. O.F. Iñigo, C. Nicolas, G. Antoni, J. Rodríguez-Aseguinolaza, A. Faik, and B. D'Aguanno: *Energy*, 2015, vol. 89, pp. 601–09.
52. O.F. Iñigo, G. Yaroslav, O. Ainhoa, P.L. Arias, J. Rodríguez-Aseguinolaza, and A. Faik: *Solar Energy*, 2017, vol. 173, pp. 152–59.
53. I. Ortega, A. Faik, A. Gil, J. Rodríguez-Aseguinolaza, and B. D'Aguanno: *Energy Procedia*, 2015, vol. 69, pp. 968–77.
54. J.C. Li, G.X. Li, F. Qiu, R. Wang, J.S. Liang, Y. Zhong, D. Guan, J.W. Li, Z.S. Li, and S. Sridhar: *Int. J. Miner. Metall. Mater.*, 2022, https://doi.org/10.1007/s12613-022-2553-x.
55. G.X. Li, J.S. Liang, J. Long, D. Guan, Z.S. Li, S. Sridhar, and J.C. Li: *ISIJ Int.*, 2022, vol. 62, pp. 1556–59.